A Percolation Model for Boiling and Predicting CHF

by

Minna Z. Wyttenbach

Submitted to the
Department of Mechanical Engineering
in Partial Fulfillment of the Requirements for the Degree of

Bachelor of Science in Mechanical Engineering
at the
Massachusetts Institute of Technology

May 2022

Signature of Author: _____
<div align="right">Department of Mechanical Engineering
May 11, 2022</div>

Certified by: _____
<div align="right">Evelyn N. Wang
Ford Professor of Engineering and Department Head of Mechanical Engineering
Thesis Supervisor</div>

Accepted by: _____
<div align="right">Kenneth Kamrin
Associate Professor of Mechanical Engineering
Undergraduate Officer</div>

A Percolation Model for Boiling and Predicting CHF

by

Minna Z. Wyttenbach

Submitted to the Department of Mechanical Engineering
on May 11, 2022 in Partial Fulfillment of the
Requirements for the Degree of

Bachelor of Science in Mechanical Engineering

Abstract

Boiling is a ubiquitous process in numerous applications, characterized by the heat transfer coefficient (HTC) and critical heat flux (CHF). Exceeding CHF can result in catastrophic failure of a system, making it an important value to understand; however, there is no universal model for predicting it. A recently investigated way to model CHF uses percolation theory, which states that CHF is reached at the percolation threshold. A bubble percolation model is used to visualize and predict boiling performance. The predictions of these models will then be used for characterizing the boiling performance of sandblasted surfaces, for which there are ongoing experiments.

Thesis Supervisor: Evelyn N. Wang
Title: Ford Professor of Engineering and Department Head of Mechanical Engineering

Acknowledgements

I would like to thank my thesis advisor Professor Evelyn Wang for her guidance and support over the last year and a half. She is an excellent role model in every regard and has made time to help me despite her very busy schedule, for which I am very appreciative.

I would also like to thank postdoctoral associate Hyeongyun Cha, from whom I have learned so much. He has served as my direct supervisor since I joined the Device Research Laboratory in February of 2021 and has been the kindest, most encouraging mentor I could ask for. He is always happy to explain concepts as many times and in as much detail as I need, while remaining patient. He is the most memorable mentor figure I have ever had and has greatly contributed to my experience at MIT. I cannot thank him enough.

I would also like to thank other members of the DRL, who have always made me feel welcome in the lab. They have been the source of many fun and interesting conversations that have made my time the DRL more memorable.

Lastly, I would like to thank the shop staff in LMP, especially Dan Gilbert, for not only allowing me to use their machines, but also helping me with whatever project I am working on when I needed it.

Table of Contents

List of Figures

1. Introduction:

1.1 Boiling Overview

Currently, many electronics are maintained at safe operating temperatures by flowing cooled air over them. However, the power density of state-of-the-art electronics is increasing exponentially and heat transfer by convection is no longer sufficient. It then follows that a cooling system with a high enough heat transfer rate is crucial in order to render cutting-edge electronics usable. Liquid-vapor phase change (boiling) is one of the most promising approaches to meet the rising demands of high heat flux electronics cooling, water treatment, and power generation because of its ability to transfer large amounts of heat with a relatively small temperature increase [1].
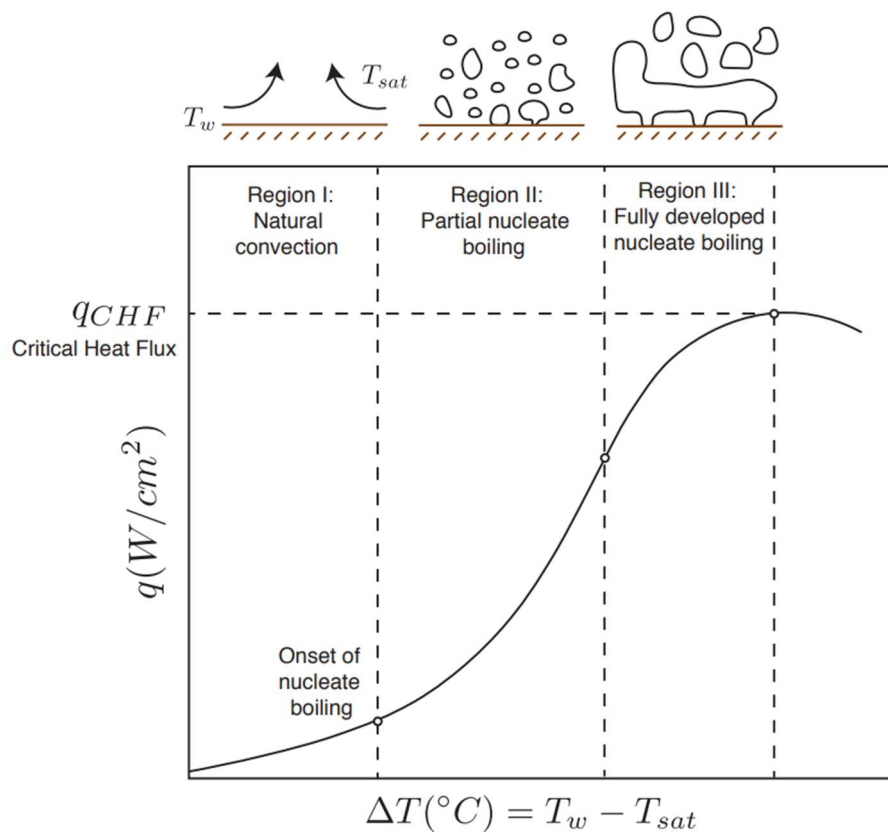
Fig. 1-1: Typical boiling heat transfer curve, showing heat flux (q) as a function of superheat $(\Delta T = T_w - T_{sat})$. Leading up to the maximum heat dissipation (CHF), we see two distinct regimes: natural convection and nucleate boiling, with the latter split further into partial nucleate boiling and fully developed nucleate boiling. Partial nucleate boiling is when individual bubbles form and leave the surface. As the heat flux increases, the nucleation site density and bubble departure radius increases, leading to bubble coalescence in the fully developed nucleate boiling regime. The difference in bubble shape between region 2 and 3 is indicated in the figure.

Flow boiling describes when flowing water is used, and it is utilized in many boiling systems. However, we will focus on pool boiling, which is when the water is contained in a given space. In pool boiling, there exist several regimes as the heat flux is increased, shown in the boiling curve in Figure 1-1.

The natural convection regime takes place at low heat fluxes. As the heat flux is increased, we see the onset of nucleate boiling, which is where isolated bubbles of vapor begin to leave the surface. In nucleate boiling, bubbles form out of nucleation sites, which may be inside of a cavity as shown in Figure 1-2. The bubble grows inside the cavity before bowing out and eventually leaving the surface. As the heat flux is further increased, the nucleation site density and bubble departure radius increase, leading to coalescence of bubbles in the fully developed nucleate boiling regime.
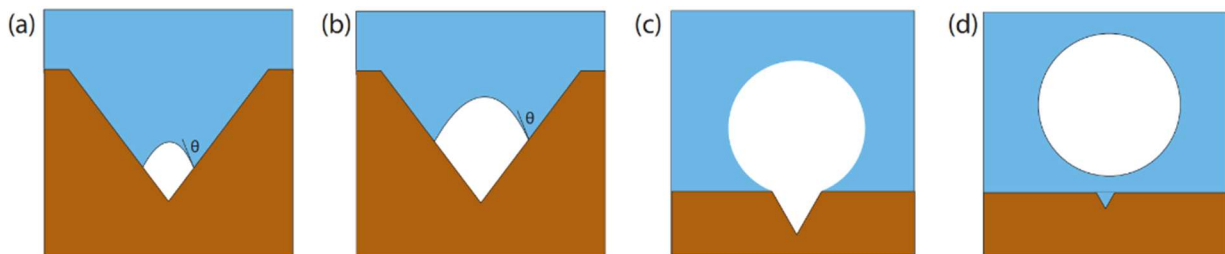
Fig. 1-2: Bubble nucleation process, showing (a-c) bubble growth and (d) departure from surface. The bubble begins to form in a surface cavity before bowing out and eventually leaving the surface. At higher heat fluxes, bubbles may coalesce.

The critical heat flux (CHF) marks the transition from nucleate boiling, where individual bubbles of vapor leave the surface, to film boiling, where the surface is covered by a vapor film. It is also the maximum heat dissipation of the system. In this film boiling regime, the temperature increases rapidly as the heat flux decreases, resulting in extremely dangerous operation conditions. This point is shown on a typical boiling curve in Figure 1-1.

The critical heat flux (CHF) is an important characteristic since it captures the maximum heat dissipation of the system and is also a point of instability above which the temperature rapidly increases.

1.2 Challenges with CHF

Since exceeding CHF leads to catastrophic failure of the system due to a rapid increase in temperature, devices that operate with high heat flux require a higher CHF such that the heat flux always remains well below it. Furthermore, additional nucleation sites are provided by microstructures of the appropriate size, increasing the heat flux.

However, predicting and enhancing boiling heat transfer performance is notoriously difficult due to the complex nature of the boiling process and still largely relies on empirical correlations and observation. Additionally, these experimental correlations are only accurate for the unique setup on which data was collected–they are not universally applicable.

1.3 Lack of CHF-Roughness or Wickability Correlations

Some literatures argue that the enhanced CHF is due to the increased three-phase contact line, implying that roughness is a major factor [2]. Others note that capillary pumping leading to quicker rewetting of the surface (hemi-wicking surfaces) is the main reason for higher CHF, meaning wickability is a major factor [3].

Song et al. performed boiling experiments on micropillar surfaces with different roughness and wickability to analyze the effect of these two parameters on CHF [4]. Their data show no clear correlation between CHF and roughness or wickability, as shown in Figure 1-3. We then look to other explanations of CHF, presented in the next section.
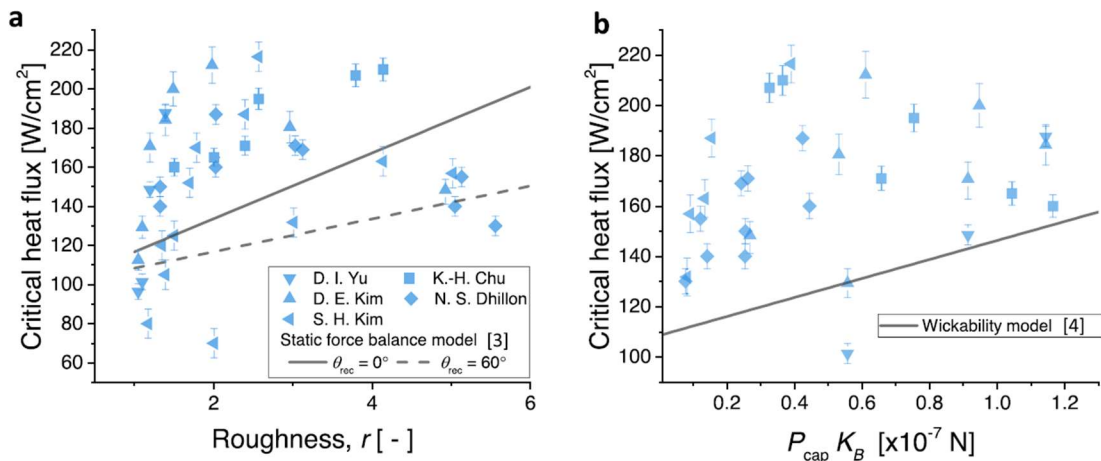
Fig. 1-3: CHF data of micropillar surfaces for past literature plotted by Song with CHF models based on (a) the roughness r and (b) the product of capillary pressure and effective permeability $P_{cap}K_B$, where P_{cap} is capillary pressure and K_B is the effective permeability. The plots show no clear correlation between CHF and r or $P_{cap}K_B$ [4].

1.4 Previous Works

Early models predicting CHF said that it occurs as a result of a hydrodynamic instability. Kutateladze approached it as a hydrodynamic phenomenon as opposed to considering individual bubble growth and departure. He postulated that CHF is reached when the velocity of the vapor leaving the heated surface reaches a critical value, causing an instability in the two-phase flow [5]. He proposed the following model for CHF using dimensional analysis:

$$q_{CHF} = K\sqrt{\rho_v}h_{fg}[\sigma g(\rho_l - \rho_v)]^{1/4} \tag{1}$$

where K is a dimensionless constant, experimentally found to be 0.16, ρ_v and ρ_l are the density of the fluid vapor and liquid, respectively, h_{fg} is the latent heat of evaporation, σ is surface tension, and g is the acceleration due to gravity.

Rohsenow and Griffith argued that CHF occurs when the distance between neighboring bubbles leaving the surface is so small that they prevent liquid from reaching the surface. The bubbles then join and form a vapor layer covering the surface [6]. They looked at the relationship between $q_{CHF}/(h_{fg}\rho_v)$ and $(\rho_l - \rho_v)/\rho_v$ and developed the following equation:

$$q_{CHF} = 0.0121\rho_v h_{fg} \left(\frac{\rho_l - \rho_v}{\rho_v}\right)^{0.6} \tag{2}$$

These models do not take into account the affinity of the liquid for the surface, nor do they consider contact angle.

Kirishenko and Cherniakov developed a model building off the critical vapor velocity theory, but incorporating contact angle, θ [7].

$$q_{CHF} = 0.171 h_{fg}\sqrt{\rho_v}[\sigma g(\rho_l - \rho_v)]^{1/4} \frac{(1 + 0.324 * 10^{-3}\theta^2)^{1/4}}{\sqrt{0.018\theta}} \tag{3}$$

Despite correctly showing decreasing heat flux with increasing contact angles, Kirishenko and Cherniakov's correlation was found not to be very accurate when tested in other setups using water as the fluid [8].

Kandlikar's model looked at force balance on a bubble and suggested that CHF occurs when the horizontal force due to vapor leaving the surface becomes larger than the forces trapping bubbles in their place, such as gravity and surface tension [9]. It explained that when gravity and surface tensions are no longer large enough to trap vapor, it will spread across the entire surface, entering film boiling and thus arriving at CHF.

$$q_{CHF} = h_{fg}\rho_v^{1/2}\left(\frac{1 + \cos\theta}{16}\right)\left[\frac{2}{\pi} + \frac{\pi}{4}(1 + \cos\theta)\cos\phi\right]^{1/2}[\sigma g(\rho_l - \rho_v)]^{1/4} \tag{4}$$

In this model, $\phi = 0$ for a horizontal upward facing surface, and $\phi = \frac{\pi}{2}$ for a vertical surface.

Jung et al. observed boiling behavior leading up to CHF using an IR camera [10]. They observed that CHF occurs when a dry patch is not able to be rewetted, and grows to cover the entire surface. At high heat fluxes, nucleation site density is large, increasing the number of dry patches on the surface. The dry patches also remain for longer and longer times, due to the speed of the advancing contact line decreasing, until they eventually grow to cover the surface. Dry patches occur due to micro-scale interactions between the fluid and the wall.

1.5 Inspiration for this Model

Recent literatures proposed that CHF is a scale-free, critical phenomena [11], as opposed to one with a macroscopic trigger , like the previously discussed papers proposed. Lloveras et al conducted an experiment with acoustic emission (AE) sensors involving placing a very hot aluminum cylinder in liquid nitrogen, inducing film boiling. They found that around CHF, the distribution of avalanches have a power law structure while the nucleate boiling and film boiling regimes do not. They then developed a spin automation model, giving the main critical exponent. Their model shows that the origin of criticality is related to a bubble percolation process.

Another experiment was performed by Charignon et al, using hydrogen near its liquid-vapor critical point, where CHF is low, dynamics are slow, and surface tension is very small [12]. They ran their experiments under reduced-gravity conditions created with magnets. They then performed analysis of dry spot areas and corroborated the previous conclusion of CHF as a scale-free phenomenon as a result of a bubble percolation process.

Zhang et al [13] performed boiling experiments on a special setup that allowed for visualization of the bubble growth process. They coated a transparent sapphire substrate with Indium-doped Tim Oxide (ITO), which served as the Joule heating element. They also installed a high speed camera that captured the infrared radiation emitted by the ITO. From this video footage, they were able to determine the nucleation site density, bubble wait time and growth time, and footprint area of each bubble at different heat fluxes. These parameters were all inputs for their simulation. Using this data, they developed a bubble percolation model showing how bubble interactions lead to the scale-free behavior at CHF. They also propose a method of predicting the CHF.

Inspired by the bubble percolation model presented by Zhang et al [13], we develop a model, where input parameters such as nucleation site density and bubble departure radius are calculated using other models and correlations from literature, as opposed to experimental data. These correlations reflect phenomena, such as a slight decrease in nucleation site density right before CHF, that the previous model does not.

In addition to the simulation, we have collected boiling data for many sandblasted surfaces with varying sandblasting parameters. Previous works have shown enhanced CHF and HTC for sandblasted surfaces, with the results of a recent paper that performed pool boiling experiments on sandblasted silicon samples shown in Figure 1-4.
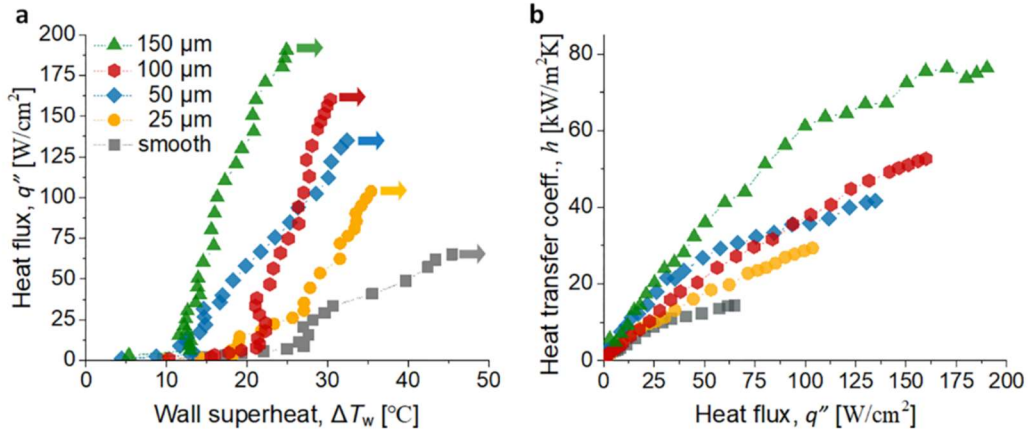
Fig. 1-4: Pool boiling results of smooth and sandblasted silicon surfaces. The sand grain size is indicated in the legend. (a) Pool boiling curves of water. (b) Heat transfer coefficient as a function of heat flux [14].

We are in the process of developing a cavity detection algorithm which would be used to predict input parameters for the simulation, allowing the extension of the model to surfaces with varying surface profiles. We also plan to experimentally validate these values by observation through a high speed camera.

2. Boiling Simulation

2.1 Nucleation Site Density

Our model was inspired by Zhang et al's percolation model [11], with the addition of nucleation site density and bubble departure diameter correlations.

Active nucleation site density N was calculated using Wang and Dhir's correlation, which related it to the critical nucleation radius, r_c [15].

$$N = 5 \times 10^5 (1 - \cos\theta)(2r_c)^{-6} \tag{5}$$

where

$$r_c = \frac{2\sigma T_s}{\rho_v h_{fg}(T_w - T_s)} \tag{6}$$

11

This correlation was developed by performing pool boiling experiments and observing through an optical microscope. Through this method they were also able to determine which nucleation sites were active. Given our sample area A, $N \cdot A$ nucleation sites were generated and randomly distributed across an ℓ-by-ℓ grid, where $\ell = 500$, with x position $= x_{pos}$ and y position $= y_{pos}$.

2.2 Bubble Departure Radius

In order to calculate the bubble radii, Cole and Rohsenow's correlation was first used to calculate a bubble radius for boiling conditions with the lowest heat flux and superheat for which isolated bubbles exist [16].

$$r_0 = \frac{A_1}{2}\left[\frac{\sigma}{g(\rho_l - \rho_v)}\right]^{1/2}\left(\frac{\rho_l c_{pl} T_{sat}}{\rho_v h_{fg}}\right)^{5/4} \tag{7}$$

where, for water, $A_1 = 1.5 \cdot 10^{-4}$ is a dimensionless constant.

Zhang et al. [13] find that the bubble radius scales with the superheat, according to the correlation in Equation 8. We scale the radius found in Equation 7 according to this correlation, yielding an average bubble radius, r_{avg}, as a function of superheat:

$$r_{avg} = r_0 \left(\frac{T_{wall} - T_{sat}}{T_{wall,0} - T_{sat}}\right)^\theta \tag{8}$$

where $T_{wall,0} - T_{sat} = 19°C$ and the contact angle $\theta = 5\pi/36$ for water. The $T_{wall,0} - T_{sat}$ value was determined experimentally by Zhang et al [13], and may change depending on the surface and liquid used.

A bubble is generated at each nucleation site with radius given in Equation 9, where d is a randomly generated number in between 0 and 1.

$$radius = \frac{\ell}{4}\sqrt{\frac{-4r_{avg}^2}{\pi}\ln(1-d)} \tag{9}$$

2.3 Matrix Representation of Bubble Growth

A meshgrid function is used to return square grid coordinates X and Y that represent all points in the ℓ-by-ℓ grid. The distance between a given nucleation site and all other points in the ℓ-by-ℓ grid is calculated using the distance formula (equation 10). If the difference between the distance and the radius of the bubble generated at that nucleation site is less than 0, that point is inside that bubble and a 1 is assigned. If it is outside that bubble, a 0 is assigned. This is repeated $N \cdot A$ times for every nucleation site.

$$dist = \sqrt{\left(X - x_{pos}\right)^2 + \left(Y - y_{pos}\right)^2} \tag{10}$$

The matrices of 0s and 1s for all bubbles are added together to yield an ℓ-by-ℓ matrix. If there is a 0 at a given point on the ℓ-by-ℓ grid, that point is not covered by a bubble; if there is a value ≥ 1, it is covered, with a number > 1 representing overlap by more than one bubble. This matrix is then thresholded and represented by an image as shown in Figure 2-1.
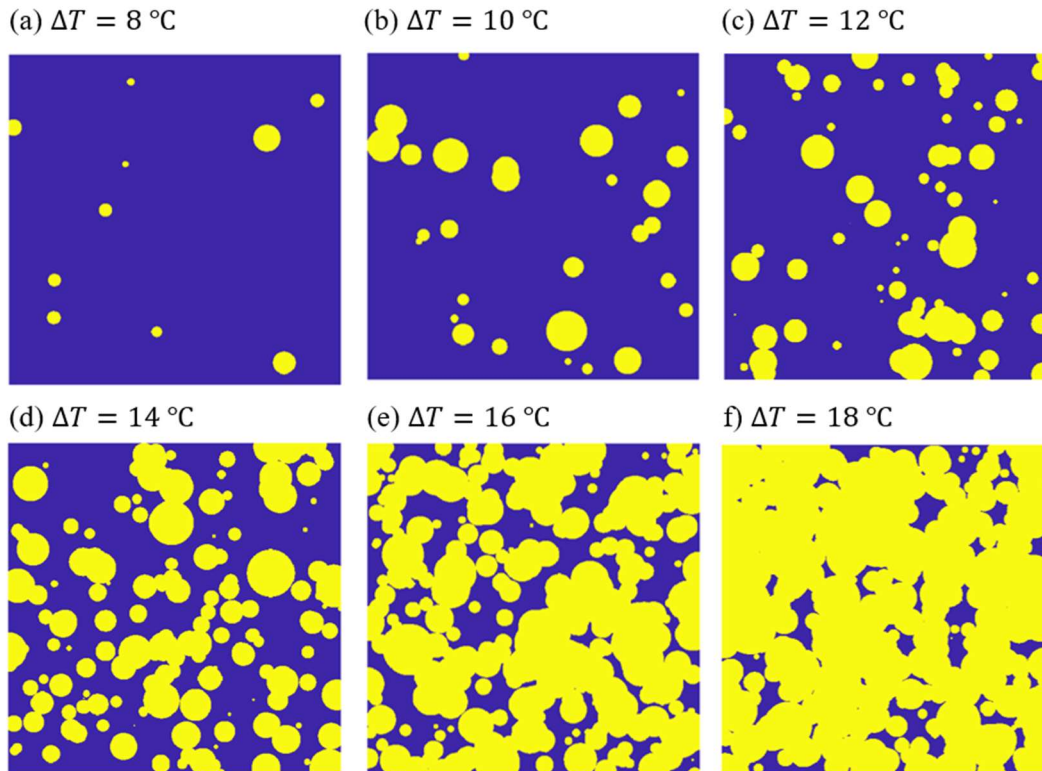

Fig. 2-1: Representative output of simulation on a 4cm x 4cm sample where wall superheat $\Delta T = (T_{wall} - T_{sat})$ is (a) 8, (b) 10, (c) 12, (d) 14, (e) 16, and (f) 18 °C. Areas in yellow and blue represent bubble footprints and the uncovered sample area, respectively.

We see that at lower heat fluxes, isolated bubbles occur. As the heat flux increases, the bubbles start to coalesce, forming larger bubble patches. At a superheat of 16 °C, corresponding to a heat flux of $\approx$80 W/cm^2, we see fewer, larger bubble patches occupy the surface. At a superheat of 18 °C, corresponding to a heat flux of $\approx$125 W/cm^2, we see one large bubble patch that occupies the majority of the surface, showing that the surface is covered by a vapor film and has reached CHF.

2.4 Percolation Model Discussion

In percolation models, each point on a grid is occupied with probability p. In this case, the grid is our ℓ-by-ℓ matrix. A cluster is defined as a group of occupied points that contain at least one occupied nearest neighbor, which in this case represents a group of bubbles that have coalesced and formed one larger bubble. The percolation threshold characterizes the transition from smaller, isolated clusters to one large cluster. The largest cluster is called the giant cluster (G), and the second largest cluster is called the second giant cluster (SG), as shown in a typical output of Zhang et al's simulation (Figure 2-2).
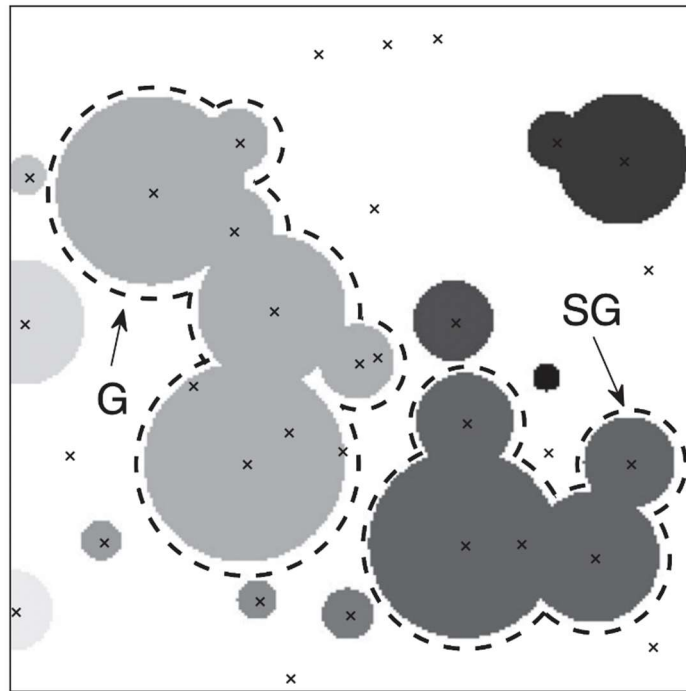

Fig. 2-2: Typical output of Zhang et al's simulation, showing the giant cluster (G) and second giant cluster (SG).

The CHF occurs at the percolation threshold, which is when SG reaches its maximum value. After this point, the largest cluster quickly spreads to cover the entire surface, marking the film boiling regime. SG was found to reach its maximum area of 1.63 cm^2 at a superheat of 17.5 °C, corresponding to a heat flux of ≈125 W/cm^2. We then have a prediction for CHF: ≈125 W/cm^2 at a superheat of 17.5 °C. Plots of G/G$_{CHF}$ and SG/SG$_{CHF}$ are presented in Figure 2-3.

From the plots we can see that initially, G and SG areas are very small, and generally the size of individual bubbles. As heat flux increases, G and SG also increase due to the coalescing of bubbles as nucleation site density and bubble departure radius increase. G and SG both continue to increase until CHF, at which SG reaches a maximum. After this point, G absorbs all other clusters, rapidly increasing until it covers the entire surface, creating a vapor layer on top of the sample.

From this we see that the percolation threshold coinciding with the max SG area is a critical point, above which the system becomes unstable. This supports the notion that CHF is a critical, percolative point in boiling. Additionally, the standard deviation of the values near CHF are high due to the very quick transition of bubble cluster formation that takes place at CHF. CHF is reached at slightly different superheats for each run, meaning that at the average some are past CHF while others have yet to reach it. Because the transition is so quick, the discrepancies between these values will be large. This divergence is characteristic of order parameters in systems at or close to critical points.

(a)

(b)
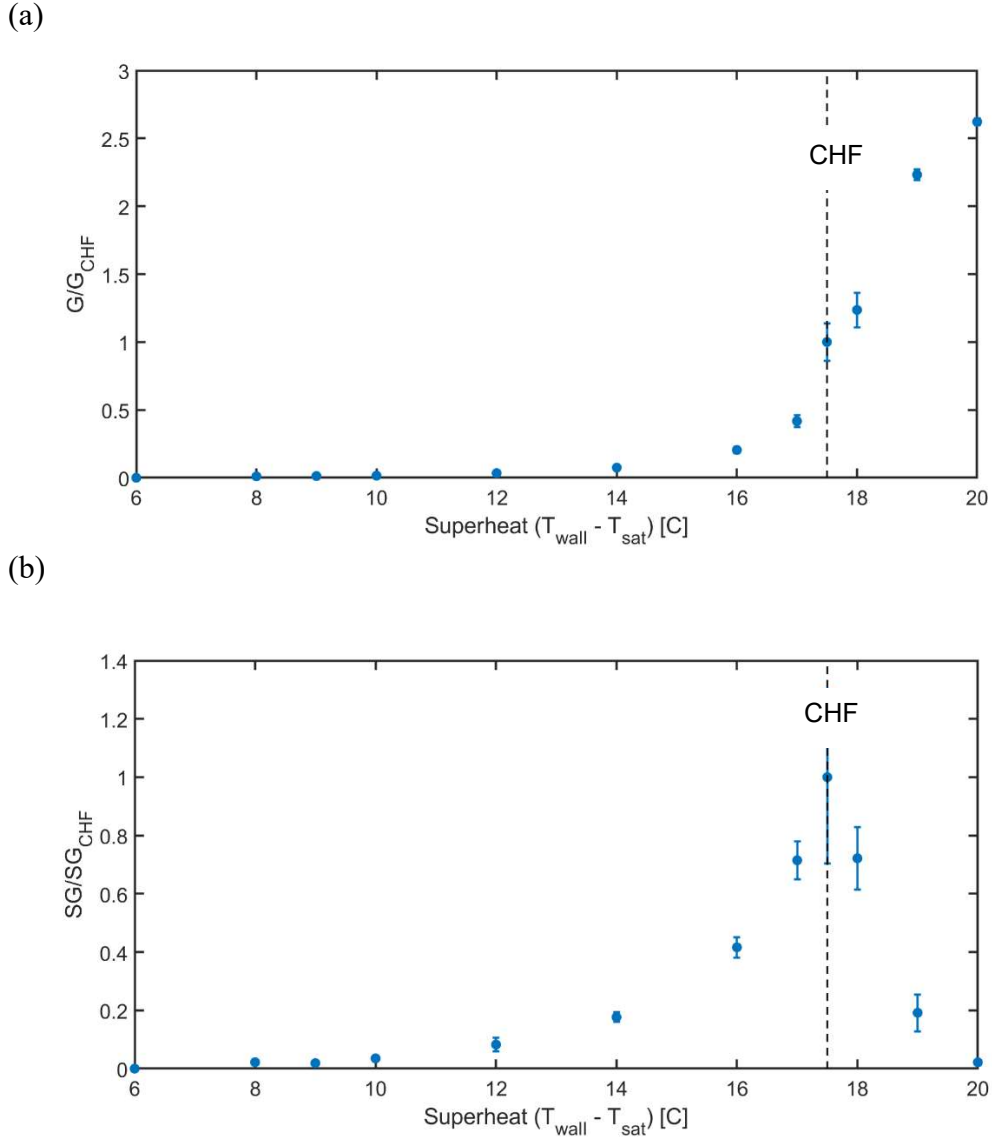
Fig 2-3: Normalized (a) giant cluster G/G_{CHF} and (b) second giant cluster SG/SG_{CHF} area as a function of the superheat. CHF is indicated with a black dashed line in both plots. The simulation was run five times for each superheat and averaged. The average value at each superheat was then divided by the average value at CHF and the standard deviation was calculated, reflected in the error bars. The standard deviation of the values near CHF is high due to the very quick transition at CHF.

3. Experiments

3.1 Experimental Setup

In the future, images and videos from a high speed camera shown in Figure 3-1 (b) can be used to acquire data from our own setups, which will then be inputs for the model. The setups consist of a copper block with cartridge heaters inside wrapped in an insulator that comes in contact with another copper block which a sample is soldered onto. The sample is placed in a chamber that is filled with water and wrapped with a rope heater. An immersion heater is also inserted. A condenser is placed on top to condense the vapor.

(a)　　　　　　　　　　　　　　　　　　　　　(b)
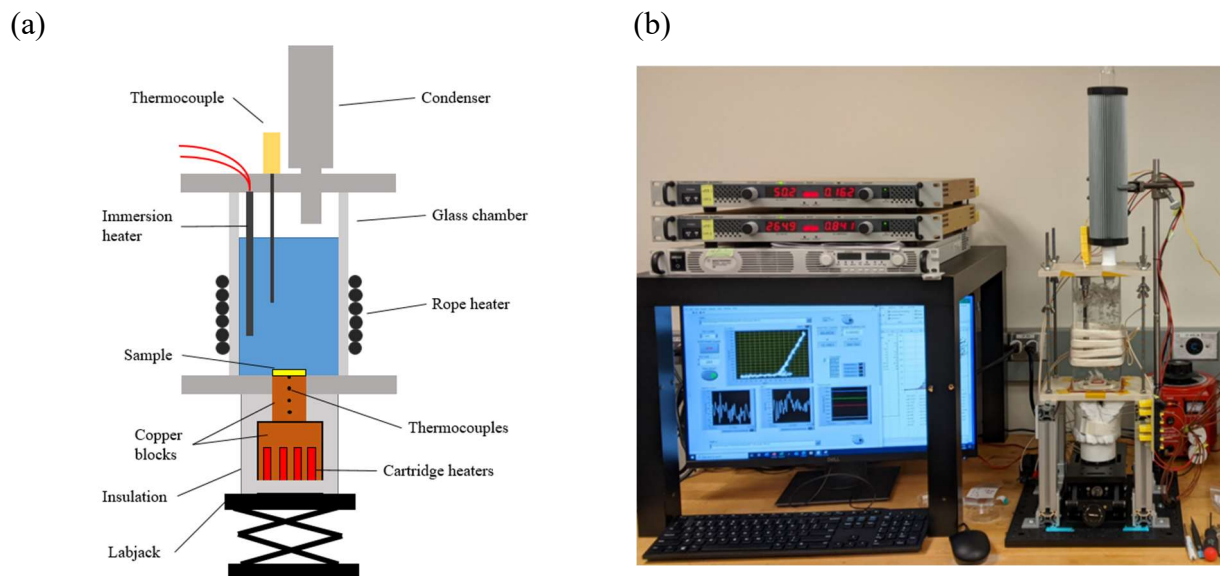
Fig. 3-1: (a) Schematic and (b) photo of boiling experimental setup. We see the chamber of water wrapped in a rope heater place atop the cartridge heaters inside the copper blocks. This is all place on a labjack. An immersion heater and additional thermocouple is inserted from the top along with the condenser. In (b) we can also see the LABView interface.

In order to measure the superheat, four thermocouples are soldered to the copper block and the heat flux q'' (W/cm^2) is calculated. The superheat and heat flux are monitored through a labview program.

Four thermocouples are inserted to the copper block that the sample is soldered onto. Three thermocouples are evenly spaced ($\Delta x = 5\ mm$) on the copper block and used to measure the temperature gradient. The heat flux is calculated using Fourier's law with a three-point backward finite difference approximation:

$$q'' = k_{Cu} \frac{3T_1 - 4T_2 + T_3}{2\Delta x} \tag{11}$$

where T_1, T_2, and T_3 are the measured temperature values at top, middle, and bottom positions as indicated on the schematic and k_{Cu} is the thermal conductivity of copper ($k_{Cu} = 2.83 \cdot 10^{-4} \cdot T^2 - 0.165T + 378.1\ W/(mK)$).

The fourth thermocouple is soldered in the interface between the top copper block and the sample and used to determine the boiling surface temperature (T_w), as shown in Eq. 12.

$$T_w = T_{tc} - \frac{q''t}{k_{Cu}} \tag{12}$$

where T_{tc} is the temperature measured by the fourth thermocouple and t is the sample thickness.

3.2 Experimental Procedure

The sample is prepared by rinsing it with acetone, isopropanol, and distilled water, and then covering the surface with 2M hydrochloric acid (HCl) for 30 seconds. This process is repeated three times before the sample is placed in a plasma cleaner for 10 minutes. Immediately after removing it from the plasma cleaner, the surface is covered with water to prevent the adsorbtion of hydrocarbons from the air. The sample is placed in the glass chamber, which is then filled with water that was previously boiled. The water is heated to 100°C and left to boil for 15 minutes to further de-gass it.

To start the experiment, the lab jack is raised to bring the two copper blocks in contact with each other. A voltage applied through the cartridge heaters is increased to raise the heat flux. A boiling curve as shown in Figure 3-2 is collected live and the heat flux is raised until CHF, at which the heater is promptly removed from the sample.
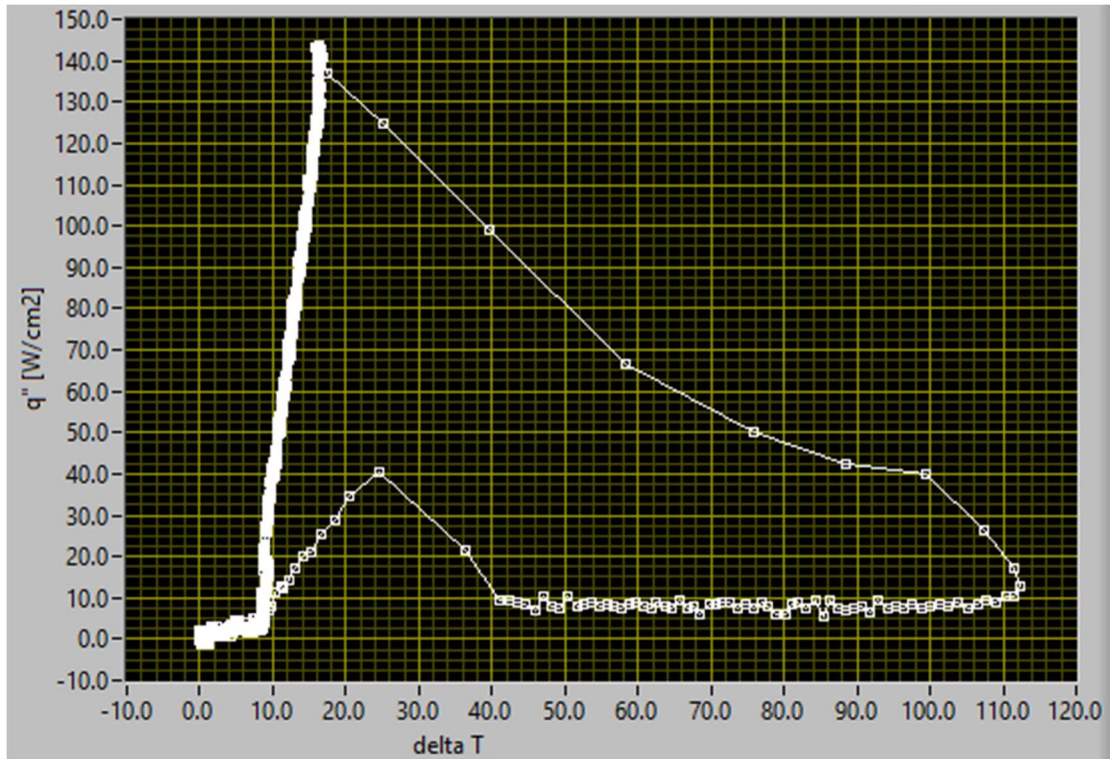
Fig. 3-2: Example boiling curve collected from our LABView setup, showing heat flux (q) as a function of superheat ($\Delta T = T_w - T_{sat}$) on sandblasted samples. We see the initial relatively flat section of the curve that is due to natural convection, and also the steep section following the onset of nucleation. The data collection stops at CHF.

3.3 Automatic Labjack

The heater is placed on an automatic labjack, which is driven by a stepper motor and lowers when a switch is flipped in order to ensure prompt removal of the heater. This is important because the temperature increases rapidly past CHF, which could result in melting of the setup if the heater is not removed quickly enough. We can see in Figure 3-2 that, despite quickly removing the heater, the temperature increases almost 100°C in around 5 seconds.

The automatic labjacks were set up according to the circuit in Figure 3-3. The circuit consists of a stepper motor connected to the automatic labjack, an Arduino Uno on which code is uploaded, an A4988 stepper motor driver, a 100 µF capacitor, and power supplies. A 12 V power supply was connected to the circuit in series, and a 5 V power supply was connected to the Arduino.

The switch is in series with the rest of the components so that when it is off, the circuit is open and the labjack will not lower. When the switch is on, the labjack will lower. The circuits for each setup are connected in parallel so that they can all operate simultaneously.

19
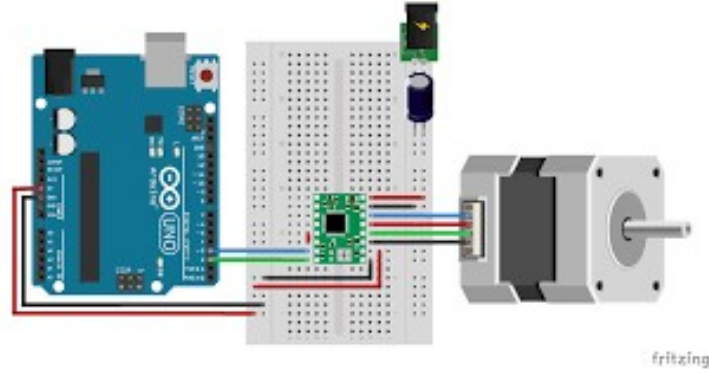
Fig. 3-3: Motorized labjack setup used to promptly remove heater from sample upon reaching CHF. The circuit consists of an Arduino Uno, A4988 Stepper motor driver, a 100 uF capacitor, and a stepper motor [17].

4. Conclusion and Future Works

We create a percolative model for boiling and predicting CHF. It was inspired by Zhang et al's work, with the addition of a nucleation site density correlation developed by Wang and Dhir and bubble departure radius correlation developed by Cole and Rohsenow, scaled for all superheats using Zhang et al's method.

Given an input superheat or heat flux, an image showing the sample bubble footprints is produced, along with the area of each cluster. We see that as the superheat/heat flux increases, more bubbles are formed with larger radii, which leads to coalescence. The area of the clusters are initially of similar size and correspond to individual bubble size. Later, some clusters are individual bubbles while others are multiple bubbles combined. The large clusters continue to grow while the smaller ones become absorbed by larger clusters. Once the second largest cluster (SG) becomes absorbed by the largest cluster (G), a point of instability is reached and G quickly occupies the entire surface. This point is the percolation threshold, or CHF.

The area of G and SG was recorded for varying superheat and heat flux. We find that the maximum SG area of 1.63 cm^2, which coincides with CHF, occurs at a superheat of 17.5 $^\circ$C and $\approx$125 W/cm^2. The results of the model support the scale-free, critical, and percolative behavior of CHF.

In the future, we plan to implement a more thorough analysis of bubble departure radius into the model, which takes into account surface features. This would allow for analysis of how roughness affects boiling and CHF according to this model. The results could then be used towards developing surfaces with high CHF.

We also plan to use a cavity detection algorithm that is being developed in parallel as an input for the model.

Appendix A

Table 1: Recorded values for G and SG area for varying superheat. Five runs are taken for each superheat, which are then averaged. The highlighted column indicates the values at CHF. The average G and SG areas for each superheat are divided by G_{CHF} and SG_{CHF}, respectively.

ΔT	0	3	6	8	9	10	12	14	16	17	17.5	18	19	20
G	0	0	0	0.1281	0.0561	0.0835	0.2271	0.3480	0.8548	2.8391	6.7028	9.1156	12.0977	14.0447
	0	0	0	0.0269	0.0820	0.1206	0.2065	0.3777	0.9248	2.9361	3.8911	6.6374	12.3458	13.8011
	0	0	0	0.0840	0.0616	0.0738	0.1567	0.3244	1.6285	1.7697	7.6847	7.6010	11.8301	14.5551
	0	0	0	0.0369	0.1140	0.0510	0.2342	0.4479	1.1192	2.0422	3.2120	5.1896	12.7842	14.0909
	0	0	0	0.0108	0.0331	0.1011	0.1022	0.5196	1.0150	1.7208	5.6069	4.9568	11.4242	14.5798
Avg. G	0	0	0	0.05734	0.06936	0.086	0.18534	0.40352	1.10846	2.26158	5.4195	6.70008	12.0964	14.21432
$\dfrac{G}{G_{CHF}}$	0	0	0	0.01058	0.01280	0.01587	0.03420	0.07446	0.20453	0.41730	1	1.23629	2.23201	2.62281
SG	0	0	0	0.1069	0.0239	0.0602	0.1898	0.2426	0.5728	1.4660	0.6648	0.7823	0.2438	0.0118
	0	0	0	0.0218	0.0313	0.1130	0.1171	0.2740	0.6836	1.0617	2.6989	1.7661	0.3889	0.0808
	0	0	0	0.0183	0.0280	0.0356	0.1237	0.2762	0.8983	0.9122	0.2413	0.8236	0.1486	0.0476
	0	0	0	0.0228	0.0484	0.0410	0.1409	0.2426	0.7071	0.9568	2.987	1.0168	0.0621	0.0276
	0	0	0	0.0093	0.0218	0.0354	0.1012	0.4036	0.5312	1.4305	1.5605	1.4942	0.7184	0.0093
Avg. SG	0	0	0	0.03582	0.03068	0.05704	0.13454	0.2878	0.6786	1.16544	1.6305	1.1766	0.31236	0.03542
$\dfrac{SG}{SG_{CHF}}$	0	0	0	0.02197	0.01882	0.03498	0.08251	0.17651	0.41619	0.71477	1	0.72162	0.19157	0.02172

References

[1]   H.J. Cho, D.J. Preston, Y. Zhu, et al., Nanoengineered materials for liquid–vapour phase-change heat transfer, *Nat. Rev. Mater.* **2016**, 2 16092.

[2]   K.-H. Chu, R. Enright, and E.N. Wang, Structured surfaces for enhanced pool boiling heat transfer, *Appl. Phys. Lett.* **2012**, 100 (24), 241603.

[3]   N.S. Dhillon, J. Buongiorno, and K.K. Varanasi, Critical heat flux maxima during boiling crisis on textured surfaces, *Nat. Commun.* **2015**, 6 (1), 8247.

[4]   Y. Song, L. Zhang, C.D. Díaz-Marín, et al., Unified descriptor for enhanced critical heat flux during pool boiling of hemi-wicking surfaces, *Int. J. Heat Mass Transfer* **2022**, 183 122189.

[5]   S. Kutateladze S, A hydrodynamic theory of changes in a boiling process under free convection, *Izvestia Akademia Nauk Otdelenie Tekhnicheski Nauk* **1951**, 4 529-536.

[6]   W. Rohsenow and P. Griffith, Correlation ofmaximum heat transfer data for boiling of saturated liquid, 1955,

[7]   Y.A. Kirichenko and P.S. Chernyakov, Determination of the first critical thermal flux on flat heaters, *Journal of engineering physics* **1971**, 20 (6), 699-703.

[8]   E. Hahne and T. Diesselhorst. Hydrodynamic and surface effects on the peak heat flux in pool boiling, in *Proceedings of the International Heat Transfer Conference Digital Library*, Begel House Inc.: **1978**.

[9]   S.G. Kandlikar, A Theoretical Model to Predict Pool Boiling CHF Incorporating Effects of Contact Angle and Orientation, *J. Heat Transfer* **2001**, 123 (6), 1071-1079.

[10]   J. Jung, S.J. Kim, and J. Kim, Observations of the Critical Heat Flux Process During Pool Boiling of FC-72, *J. Heat Transfer* **2014**, 136 (4).

[11]   P. Lloveras, F. Salvat-Pujol, L. Truskinovsky, et al., Boiling Crisis as a Critical Phenomenon, *Phys. Rev. Lett.* **2012**, 108 (21), 215701.

[12]   T. Charignon, P. Lloveras, D. Chatain, et al., Criticality in the slowed-down boiling crisis at zero gravity, *Phys. Rev. E* **2015**, 91 (5), 053007.

[13]   L. Zhang, J.H. Seong, and M. Bucci, Percolative Scale-Free Behavior in the Boiling Crisis, *Phys. Rev. Lett.* **2019**, 122 (13), 134501.

[14]   Y. Song, C. Wang, D.J. Preston, et al., Enhancement of Boiling with Scalable Sandblasted Surfaces, *ACS Appl. Mater. Interfaces* **2022**, 14 (7), 9788-9794.

[15]   C.H. Wang and V.K. Dhir, Effect of Surface Wettability on Active Nucleation Site Density During Pool Boiling of Water on a Vertical Surface, *J. Heat Transfer* **1993**, 115 (3), 659-669.

[16]   R. Cole and W. Rohsenow. Correlation of bubble departure diameters for boiling of saturated liquids, in *Proceedings of the Chem. Eng. Prog. Symp. Ser*, 211 213: **1969**, 65, pp 211-213.

[17]   A.B.d. Bakker. *A4988 Stepper Motor Driver with Arduino Tutorial*. [retrieved May 5, 2022]; Available from: https://www.makerguides.com/a4988-stepper-motor-driver-arduino-tutorial/.